PASJ: Publ. Astron. Soc. Japan **63**, 31–44, 2011 February 25

New Distance and Revised Natures of High-Mass Star Formation in G5.89−0.39

Kazuhito MOTOGI,[1] Kazuo SORAI,[1,2] Asao HABE,[1,2] Mareki HONMA,[3,4] Hideyuki KOBAYASHI,[3,4,5] and Katsuhisa SATO[4]
[1]*Department of Cosmosciences, Graduate School of Science, Hokkaido University, N10 W8, Sapporo, Hokkaido 060-0810*
motogi@astro1.sci.hokudai.ac.jp
[2]*Department of Physics, Faculty of Science, Hokkaido University, N10 W8, Sapporo, Hokkaido 060-0810*
[3]*Mizusawa VLBI Observatry, National Astronomical Observatory, 2-12 Hoshi-ga-oka, Mizusawa-ku, Oshu, Iwate 023-0861*
[4]*Department of Astronomical Sciences, Graduate University for Advanced Studies, 2-21-1 Osawa, Mitaka, Tokyo 181-8588*
[5]*Department of Astronomy, Graduate School of Science, The University of Tokyo, 7-3-1 Hongo, Bunkyo-ku, Tokyo 113-0033*

(Received 2010 August 14; accepted 2010 December 15)

Abstract

We report on astrometric observations of the 22 GHz H_2O masers in the high-mass star-forming region G5.89−0.39 with VERA (VLBI Exploration of Radio Astrometry). A newly derived distance of $1.28^{+0.09}_{-0.08}$ kpc is the most precise, and is significantly nearer than the previous values. We revised the physical parameters and reconsidered the nature of G5.89−0.39 based on the new distance as follows: (1) The ionizing star of the ultra compact (UC) H II region is a late O-type (O8–O8.5) zero age main sequence (ZAMS) star, consistent with previously established limits based on its infrared spectral line emission. (2) Crescent-like maser alignment at the position of the O-type ZAMS star may trace an accretion disk (or its remnant), which suggests that the star is still young, and before complete evaporation of circumstellar materials. (3) Although the revised mass for the east-west outflow has been reduced, it is still quite large ($100\,M_\odot$), which indicates that a significant fraction of the mass is entrained material, and that the dynamical age significantly underestimates the actual outflow age. Our newly-derived distance emphasizes that G5.89−0.39 is one of the nearest targets to investigate ongoing high-mass star formation and evolution in a compact cluster containing a young O-type star.

Key words: astrometry — ISM: H II regions — ISM: individual (G5.89−0.39, W28A2) — ISM: jets and outflows — masers (H_2O)

1. Introduction

A systematic and consistent scenario of high-mass star formation has not yet been constructed. In spite of enormous and intense work, there are many hypotheses and unsolved issues (e.g., Zinnecker & Yorke 2007 and reference therein). But, several recent theoretical studies have suggested that high-mass star formation can be achieved via mass accretion (e.g., Krumholz et al. 2009). This hypothesis seems to be consistent with observational signatures of a massive accretion disk and a torus around a high-mass protostellar object (HMPO) or protocluster (e.g., Beuther et al. 2009). Upcoming Atacama Large Millimeter / submillimeter Array (ALMA) will be able to sufficiently resolve such a circumstellar structure, and provide more quantitative information about a specific accretion mechanism onto an individual HMPO.

A precise distance of a source is essential for any quantitative discussions. However, most of the high-mass star-forming regions, which will be targets for ALMA, are even located on the inner galactic plane, where source distances often contain significant uncertainty. Direct distance measurements by astrometric observations are quite important for such regions, especially in highly accurate VLBI (Very Long Baseline Interferometry) astrometry, which is the only technique sufficiently suitable for deeply embedded high-mass star-forming regions where optical measurements are almost impossible. Hachisuka et al. (2006) first demonstrated great performance of VLBI astrometry using a H_2O maser in the W3(OH) region; since then, several studies have achieved 10 micro-arcsecond (μas) accuracy for northern star-forming regions (e.g., Moellenbrock et al. 2009; Sato et al. 2010a). In this paper, we report on an annual parallax measurement of H_2O masers in the high-mass star-forming region G5.89−0.39 with VERA (VLBI Exploration of Radio Astrometry: Kobayashi et al. 2008).

G5.89−0.39 (also known as W28A2) is one of the most famous, shell-type ultra-compact (UC) H II regions (e.g., Wood & Churchwell 1989). An O-type ionizing star has been detected as a near-infrared (NIR) point source by Feldt et al. (2003) inside the shell (hereafter Feldt's star). Acord, Churchwell, and Wood (1998) (hereafter ACW98) have directly measured the dynamic angular expansion of the radio shell. The observed supersonic expansion and short dynamical age (600 yr) indicate that this small UCH II region is just after the birth. G5.89−0.39 is also known to be a host of an extremely massive outflow, which is centered on the shell (e.g., Acord et al. 1997). The whole part of the shell is completely inside the outflow extent (e.g., Watson et al. 2007). This also gives further support on the remarkable youth of the UCH II region.

Previously reported distances for G5.89−0.39 vary over a wide range (1.9–3.8 kpc: Hunter et al. 2008, and reference therein). Almost all of them were measured through the kinematic distance method, but at a galactic longitude of 5.°89, this method intrinsically contains a large systematic error of kpc order. Although ACW98 tried to estimate the distance from

Table 1. Summary of obsevations.

Date	Synthesized beam (mas × mas)	PA (°)	Resolution (km s^{-1})	1-σ Noise* (Jy beam^{-1})	DN_p† / DN_s (σ)	Comments for T_{sys}
2007/11/5	1.92 × 0.71	−24.33	0.21	0.82	9 / 32	∼5000 K at IR‡
2008/1/12	1.88 × 1.02	−16.23	0.21	0.35	11 / 166	∼1000 K at IS
2008/3/14	2.15 × 0.88	−20.15	0.21	0.22	15 / 402	—
2008/5/7	2.32 × 0.88	−24.48	0.42	0.63	14 / 530	500–2000 K at OG
2008/7/1	2.14 × 0.81	−23.04	0.21	0.42	8 / 128	—
2008/11/11	2.62 × 0.84	−26.16	0.21	0.29	11 / 144	800–3000 K at OG
2009/2/6	2.02 × 0.92	−16.82	0.21	0.17	15 / 255	—
2009/5/18	2.26 × 0.84	−23.32	0.21	0.28	15 / 43	—
2009/9/13	2.21 × 0.78	−19.95	0.21	0.25	— / 54	—

* Typical value in self-calibrated images.
† The maximum dynamic ranges for phase-referenced (DN_p) and self-calibrated image (DN_s).
‡ IR, IS, OG: Iriki, Ishigaki, Ogasawara station, respectively.

the shell expansion without any galactic rotation models, they still have adopted several assumptions for their modeling of the data. From this point of view, our direct distance measurement is very important to confirm the physical parameters of G5.89−0.39.

2. VERA Observations

VERA observations of the H_2O masers ($J_{K_aK_c} = 6_{16}$–5_{23}) at 22.23508 GHz associated with G5.89−0.39 have been carried out at 9 epochs between 2007 November and 2009 May. A summary of all observations is listed in table 1, which contains observing dates, synthesized beam sizes in milli-arcsecond (mas), beam position angles (PA) east of north, spectral resolutions, typical noise levels and dynamic ranges of synthesized images and brief comments, if any, about system noise temperatures (T_{sys}).

Each observation was made in VERA's dual-beam mode in which a targeted maser source and a phase calibrator (or position-reference source) were observed simultaneously (Kawaguchi et al. 2000; Honma et al. 2003). The real-time, instrumental phase difference between the two beams, was measured for a calibration using artificial noise sources during the observations (Honma et al. 2008a). We chose J1755−2232 ($\alpha_{2000} = 17^h55^m26^s.2848$, $\delta_{2000} = -22°32'10''.61656$: Petrov et al. 2005) as a paired calibrator. This source is separated from G5.89−0.39 by 1°.92 at a position angle of −140° east of north. The flux density of J1755−2232 is about 150 mJy. No significant structure is seen in this point-like calibrator. A bright calibrator, NRAO530 (= J1733−1304: Ma et al. 1998), was also scanned every 120 minutes as a delay and bandpass calibrator. Each observation was made for about 6 hours, but the total scan time for the targeted source pair was only about 2.5 hours because we observed not only the G5.89−0.39–J1755−2232 pair, but also another maser–calibrator pair alternately. We will describe another source pair in a forth-coming paper.

Left-handed circular polarized signals were quantized at 2-bit sampling and filtered with the VERA digital filter unit (Iguchi et al. 2005); after that, data were recorded onto magnetic tapes at a data rate of 1024 Mbps. There were 16 IF channels with a 16 MHz band width, where one IF was assigned to the maser lines, and the other 15 IF of total 240 MHz were assigned to J1755−2232 and NRAO530. A data correlation was performed with the Mitaka FX correlator (Chikada et al. 1991). Correlated data were divided into 512 and 64 spectral channels for the maser and calibrators, respectively. For the maser lines, the full 16 MHz data were used only in the fourth epoch, and in other cases we used 8 MHz, which is enough to cover all master emissions and provides a sufficient velocity resolution (0.21 km s^{-1}).

The system noise temperatures depended on the weather conditions at each station and elevations. The typical T_{sys} value at an averaged elevation angle was varied over 200 to 500 K for each station in the case of normal weather. Sometimes it exceeded 1000 K in a bad case for Ogasawara and Ishigaki station. There was a very high T_{sys} value (∼5000 K) at Iriki station in the first epoch, and hence we performed phase-referenced imaging using three other stations in this epoch. Phase-referenced images of the targeted maser source were successfully obtained in 8 epochs without the final epoch, where significant phase fluctuations still remained after a fringe fitting for J1755−2232, and then all maser spots were completely defocused.

3. Data reduction

Data reduction was carried out using the NRAO Astronomical Imaging Processing System (AIPS) package. Amplitude and bandpass calibrations were made for the targeted maser and J1755−2232 independently. We calibrated the clock parameters for each station using the residual delay of NRAO530. The tropospheric zenith delay offset was also calibrated by modified delay-tracking data, which were calculated based on actual measurements of the atmospheric zenith delay with the global positioning system (GPS) at each station (Honma et al. 2008b).

There were two different paths of the analysis, depending on the purpose. The one was phase-referencing (or 2-beam) analysis for a measurement of the annual parallax, and another was single-beam analysis, which was suitable for searching all maser spots and studying their internal motion. Here, the term 'maser spot' indicates a maser component seen in a single

velocity channel and, in contrast, the term 'maser feature' represents a physical gas clump that consists of several maser spots detected in successive velocity channels, and located close to each other. We define it in the same way as Motogi et al. (2008).

In a single beam analysis, we simply performed fringe fitting and self-calibration using the brightest maser spot in feature O1 (see subsection 4.3). We then searched for all maser spots by a wide-field mapping under a 7-σ detection limit. The total explored area was $5'' \times 5''$ of each channel map centered on the ionizing star in G5.89−0.39. The annual aberration was also corrected for several masers that were significantly distant ($\gg 3''$) from the phase-referenced maser spot in this analysis.

In the phase-referencing analysis, fringe fitting and self-calibration for J1755−2232 were done; then, the obtained delay, rate and phase solutions were applied to the target visibilities following a correction of the measured instrumental phase difference between the two beams (see above). The modified delay-tracking mentioned above was re-calculated with respect to each maser feature for accurate position measurements. A new delay-tracking center was always located within 10 mas from the relevant maser feature.

The coherence in phase-referenced images were still significantly degraded at this stage. Because of the low brightness and large separation angle of J1755−2232, and the low elevation angle during observations, significant atmospheric zenith delay residuals, which were a main cause of the coherence loss, still remained. We, therefore, estimated and corrected those residuals with the image optimizing method described in Honma et al. (2007, 2008b). The estimated residuals were found to be within ± 3 cm in all epochs (~ 1.5 cm on average). This is consistent with a typical case seen in VERA observations (Honma et al. 2008b). The dynamic ranges (or signal to noise ratios) of phase-referenced images showed a dramatic improvement with this correction. However, even after this improvement, limited coherence and defocusing made several faint spots undetectable.

After these calibrations, a synthesized image cube was finally made with all maser features in both analyses. Each cube had a field of view of 25.6 mas × 25.6 mas centered on a relevant feature. Imaging and deconvolution (CLEAN algorithm) was done in uniform weighting, which provided the highest spatial resolution. The synthesized beam was about 2.2 mas × 0.9 mas with a position angle of $-20°$. The typical image noise level was ~ 400 mJy beam^{-1} (1-σ) in the case of single-beam analysis (see table 1). It was significantly increased in the phase-referenced case by a factor of 2 or 3, and up to 10 in the worst case. The absolute and relative positions of each maser spot were determined by an elliptical Gaussian fitting. The formal error in this fitting was typically 50 μas in RA and 100 μas in Dec. This value is approximately equal to the uncertainty of the relative positions between each maser spot. An overall discussion about the accuracy of the absolute positions in each measurement is given in subsection 4.2.

4. Result

4.1. Parallax Measurement

There were two strong maser features (feature O1 and C6 in subsection 4.3) successively detected for 8 epochs in phase-referenced maps. We measured their absolute motions referenced on J1755−2232. These motions can be expressed by the sum of the annual parallax, π, and the proper motion of each feature, μ. The latter is usually assumed to be a linear and constant motion for simplicity (e.g., Nakagawa et al. 2008). This seems to be applicable for our case, because the relative proper motion between the two features are actually fitted by a linear motion (see subsection 4.3 and figure 2), and the drifts of their line-of-sight velocities were very negligible (< 0.2 km s^{-1}) during the two years.

A least-squares fitting was made with π plus μ to the right-ascension offsets ($X \equiv \Delta\alpha \times \cos\delta$) from the first epoch. We performed our fittings in the same way as Hirota et al. (2008). Here, all detected maser spots in each feature (7 maser spots per feature) were distinctly used, and the initial position of each maser spot, X_0 and Y_0, was included as a fitting parameter. The reduced χ^2 was calculated as

$$\chi^2 = \frac{1}{m} \sum_i \omega_i \left[X_i - f(t_i) \right]^2 , \quad (1)$$

where m and ω_i are the degree of freedom and a fitting weight for each data point, respectively. We adopted a dynamic range of a phase-referenced image (DN) as a fitting weight, since it was a rough measure of the coherence loss caused by any residual delay, which was difficult to estimate directly. A weight for the i-th data point was to be $\omega_i \propto \mathrm{DN}_i$ and scaled to make the total reduced χ^2 to be ~ 1. If we assume the normal distribution, $1/\sqrt{\omega_i}$ is equal to the error variance of the i-th data point.

Figure 1 shows examples of the parallax measurement for G5.89−0.39. Note that only a linear proper motion was fitted to the declination offsets ($Y \equiv \Delta\delta$), since G5.89−0.39 was located on the ecliptic plane ($\beta \sim -0.^\circ 6$), where the parallax in the declination degenerated into an order of 10 μas. It is just comparable with the maximum accuracy of VERA's dual beam astrometry (Honma et al. 2007), and is hard to detect. In each figure, the associated error bars indicate $1/\sqrt{\omega_i}$ values. The X values were well fitted by a linear motion (dashed line) and parallax (solid curve); in contrast, large dispersion from the best-fit linear motion is clearly seen in cases of Y. The error in Y (~ 0.9 mas) is, in fact, much larger than that in X (~ 0.4 mas) as well as several other observations with VERA (e.g., Hirota et al. 2007). A detailed analysis about these errors is given in the next subsection.

Table 2 presents a summary of these fittings. The presented σ values are rms deviations of post-fit residuals, which are good measures of the typical error for each measurement. Because both of the features O1 and C6 seem to be associated with a single UCH II region, we can assume that they show the same annual parallax within the astrometric accuracy of VERA. Thus, the best-fit annual parallax was estimated to be $\pi = 0.78 \pm 0.04$ mas, corresponding a distance of $1.28^{+0.07}_{-0.06}$ kpc from the Sun, by the weighted-means of those for the two features.

One can see that some data points are not included within the 1-σ error range in figure 1. This can be due to inequable data quality in each observing epoch. We, hence, performed a bootstrap analysis to test such an effect, where data for each

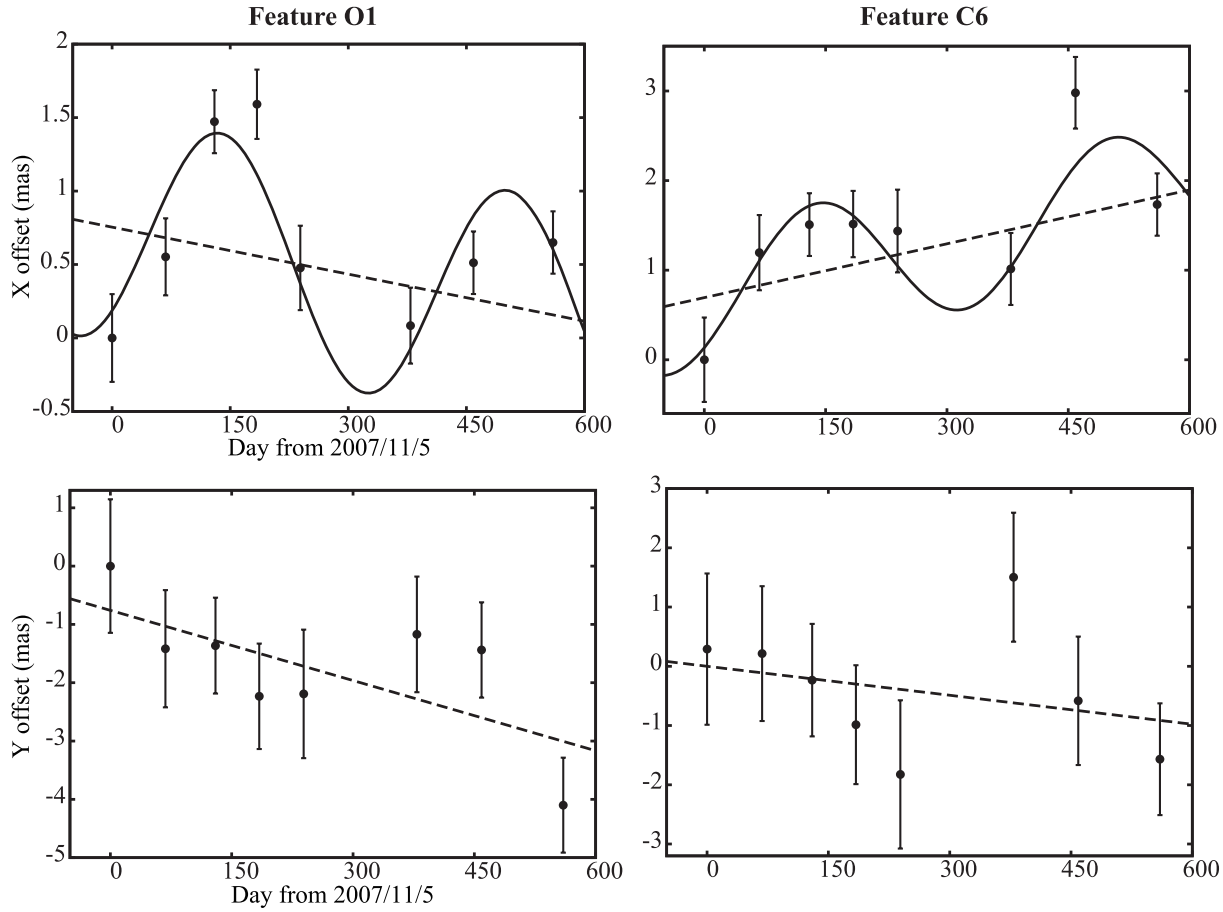

Fig. 1. Examples of parallax fitting for the brightest maser spot of feature O1 (left) and C6 (right). Here, the X and Y axes show the elapsed days from the first epoch and positional offsets from $\alpha_{2000} = 18^{\rm h}00^{\rm m}30\overset{\rm s}{.}3066$, $\delta_{2000} = -24°04'04\overset{''}{.}48649$ in mas, respectively. The annual parallax (solid curve) and linear proper motion (dashed line) were successfully fitted in the X direction (upper two panels). On the other hand, only a linear proper motion was fitted in the Y direction because of the location of G5.89−0.39 (see text). The errors in each panel were calculated from the fitting weights, which were scaled to make the total reduced χ^2 to be ~ 1.

Table 2. Summary of simple parallax fittings.

Feature	$V_{\rm LSR}$ (km s^{-1})		π (mas)	D (kpc)	σ^* (mas)	$\mu^\dagger$ (mas yr^{-1})
O1	9.4	X	0.79 ± 0.05	1.27 ± 0.08	0.27	-0.43 ± 0.09
		Y	—	—	0.78	-1.43 ± 0.29
C6	11.0	X	0.77 ± 0.09	$1.30^{+0.17}_{-0.14}$	0.39	0.77 ± 0.14
		Y	—	—	0.94	-0.47 ± 0.30
		Combined‡	0.78 ± 0.04	$1.28^{+0.07}_{-0.06}$		

* The rms deviations of the post-fit residuals.
† 1 mas yr^{-1} = 6.1 km s^{-1} at the distance.
‡ The weighted means of those for two features.

maser spot were randomly resampled 10000 times, and a least-squares fitting was iteratively performed for each dataset.

The obtained frequency distributions of π were well fitted by a Gaussian. Detailed parameters are presented in table 3. The resultant error of ± 0.05 mas is slightly larger than that of simple fittings, but is almost consistent with it; we finally took it as a conclusive 1-σ error of our parallax measurement. We also emphasize that even if we adopt a 3-σ error ($> 99\%$ confidence), the equivalent distance range is still significantly nearer than previously reported values.

4.2. *Astrometric Error Sources*

The post-fit residuals seen in our parallax and proper-motion measurement are much larger than the formal errors of the elliptical Gaussian fittings. This can be seen especially in the Y fitting, where the residual variance is about 850 μas. We again note that the parallax in Y degenerated into negligible order because of the source location. This fact suggests

Table 3. Gaussian Parameters of the π distributions from a bootstrap analysis.

Feature	Median (mas)	Standard deviation	D (kpc)	3-σ*
O1	0.80 ± 0.005	0.06 ± 0.005	$1.25^{+0.11}_{-0.09}$	$^{+0.38}_{-0.24}$
C6	0.75 ± 0.008	0.10 ± 0.008	$1.33^{+0.20}_{-0.15}$	$^{+0.87}_{-0.38}$
Combined†	0.78	0.05	$1.28^{+0.09}_{-0.08}$	$^{+0.33}_{-0.22}$

* 3-σ (> 99% confidence) error ranges in kpc.
† The weighted means of those for two features.

that Y fluctuations from a simple linear motion directly reflect the degree of the actual error in each position measurement. One of the main sources of this error is thought to be atmospheric zenith delay residuals, as discussed in several studies with VERA (e.g., Sato et al. 2008 and references therein). We first checked this in our case using several expressions from Nakagawa et al. (2008).

They assumed the error in the station positions and image quality of a phase-referenced map as additional error sources. The former is only about 7 μas with a separation angle of 1.°92 and a baseline error of 3 mm, which is the typical value for VERA. This is, of course, negligible in our case. The latter can be expressed by the relevant beam size in the X and Y directions divided by the dynamic range of an image. The beam-position angles are almost parallel to the Y direction in our observation, and thus the expected error is 80 μas in X and 200 μas in Y. On the other hand, an error caused by the atmospheric zenith delay residual is proportional to the difference of the signal path length between 2 beams divided by the relevant baseline length. This can be calculated from the atmospheric zenith delay residual, the typical zenith angle and the separation angle of the sources [see equation (1) in Nakagawa et al. 2008]. If we adopt a residual of 3 cm as an upper limit in our case and average zenith angle of 65°, the atmospheric error is about 330 μas in X and 820 μas in Y. This is almost consistent with the result of Monte-Calro Simulations in Honma et al. (2008b).

Because J1755−2232 appears to be an ideal point source, the internal structure of J1755−2232 does not cause significant error. If we also assume that the effect of the internal structures of the maser features is also negligible for simplicity, we finally obtain a total error of 340 μas and 850 μas in each direction from the root sum square of these 3 values. As one can see that this is consistent with the standard deviation of the post-fit residuals (see table 2). If the differences of a separation angle, pair position angle and zenith delay residuals are taken into account, this can be roughly comparable to the value in Choi et al. (2008), where the source declination is almost the same as in our case. However, the expected error of the parallax is estimated to be ~ 0.09 mas in a statistical way; here, we divide 340 μas by $\sqrt{2 \times (8-1)}$ while considering 8 observing epochs and 2 distinct maser features. This is clearly larger than the actual fitting errors of a least-squares analysis (0.04 mas).

This seems to indicate that the effect of the variability of the maser feature structures, which we ignored above, cannot be negligible. This type of error is another important error source for VERA observations (e.g., Hirota et al. 2007). Moreover, it can actually be a dominant error source in some cases (e.g., Sato et al. 2008). If we attribute the dominant part of the post-fit variance to this effect, instead of the atmospheric error, the expected error of the parallax can be reduced by an additional factor of $1/\sqrt{N}$; here, N is the number of maser spots in a single feature. Since both feature O1 and C6 consist of 7 maser spots in our case, the conclusive error of parallax is though to be $0.33/\sqrt{7 \times 2 \times (8-1)} \sim 0.03$ mas, where the numerator of 0.33 mas is the averaged value of the post-fit residual in X. This is just comparable to the actual fitting error.

Therefore, we conclude that the dominant error source is the variability of the maser feature structures in our case, although the contribution from atmospheric zenith delay residuals is also nonnegligible. The proportion of their contributions is, more quantitatively, believed to be $\sim$2:1, if we use averaged atmospheric delay residuals of ~ 1.5 cm, which was evaluated from the image optimizing method.

4.3. Kinematics and Spatial Distribution of Masers

The absolute proper motions of features O1 and C6 shown in table 2 are motions with respect to the Sun, and hence include the contribution of solar motion and the galactic rotation. If we assume the solar motion relative to the LSR based on the Hipparcos data (Dehnen & Binney 1998), the contribution of solar motion is calculated to be 0.69 mas yr^{-1} and -1.19 mas yr^{-1} for X and Y, respectively. The contribution of the galactic rotation is estimated to be -0.04 mas yr^{-1} and -0.07 mas yr^{-1} based on a R_0 of 8.4 kpc and Θ_0 of 254 km s^{-1} (Reid et al. 2009). This value is very negligible and do not change in the common range of R_0 and Θ_0 (220–254 km s^{-1}, 8.0–8.5 kpc: Hou et al. 2009). Here, we assumed flat rotation, and adopted our newly determined distance of 1.28 kpc. The intrinsic proper motions of the maser features, where these two contributions are subtracted, is represented in table 4. We note that these motions are still included the peculiar motion of their natal cloud and the internal motions of each maser feature. Since only two features are detected in 2-beam analysis, we cannot divide these two components at this section, but a brief presumption will be provided in sub-subsection 5.2.2 based on model fitting of the maser kinematics.

An additional 12 maser features were detected in the single beam analysis. All parameters of the detected features are listed in table 5. A total of 14 maser features can be divided into 4 maser sites. We name these sites as origin (O), center (C), north (N), and south (S) based on their positions. These four maser sites are widely spread around the UCH II region. We estimated the internal proper motions relative to the phase-referenced feature, O1, for the features that were detected in at least three observing epochs. Figure 2 shows an

Table 4. Intrinsic proper motions.*

Feature	Absolute proper motion†		Relative proper motion†	
	μ_X	μ_Y	μ_X	μ_Y
O1	-1.08 ± 0.24	-0.16 ± 0.40	—	—
C6	0.12 ± 0.29	0.79 ± 0.47	—	—
O2	-1.02 ± 0.33	-0.46 ± 0.43	0.06 ± 0.09	-0.29 ± 0.03
C6	-0.21 ± 0.29	1.31 ± 0.48	0.87 ± 0.05	1.47 ± 0.08
C9	-1.51 ± 0.27	0.72 ± 0.53	-0.43 ± 0.03	0.89 ± 0.13
N	-3.38 ± 0.43	-1.79 ± 1.56	-2.3 ± 0.19	-1.63 ± 1.16
S1	-0.12 ± 0.40	-1.03 ± 0.93	0.96 ± 0.16	-0.86 ± 0.53

* The upper 2 rows are from the parallax fitting. The lower 5 rows are from the internal proper motions relative to O1.
† All values are in the units of mas yr^{-1}.

example of feature C6. Their internal motion was well-fitted by linear motion. Estimated motions are also summarized in table 4. The overall distributions and proper motions of the maser features are represented in figure 3, where black and grey arrows show the relative and converted absolute proper motions, respectively. The relative positions and internal proper motions of all maser features were converted to absolute values using the position and motion of the feature O1. The converted motion of C6 actually coincides with the directly estimated one within the error.

Each of the sites O, N, and S, which are located outside of the ionized shell, contains only one or two maser features. This limited number of maser features can be related to the lifetime of H_2O maser activity. They are generally believed to disappear along with the evolution of the UCH II region (e.g., Beuther et al. 2002a; Breen et al. 2010), in attributing to a dispersion of dense gas, which is required to excite masers. All of these sites are associated with SiO $J = 8$–7 emission detected by Sub-Millimeter Array (SMA) (Hunter et al. 2008). SiO $J = 8$–7 emission is a moderate shock tracer, and is frequently observed in post-shock gas that is associated with a protostellar outflow (e.g., Takami et al. 2006). Such a spatial relationship may indicate that H_2O maser and SiO emission trace the same shock fronts. This is not so surprising because H_2O masers are also associated with strong outflow shock frequently (e.g., Motogi et al. 2008; Torrelles et al. 2010).

On the other hand, the line-of-sight velocities of the maser features in the sites O and N are not consistent with that of SiO emission. The velocity offsets are larger than 5 km s^{-1}. These offsets may reflect the difference of precise locations where each emission comes from. This can be simply attributed to the different excitation conditions of SiO and H_2O. The critical density of SiO $J = 8$–7 emission is $n_{H_2} \cong 10^7$ cm^{-3}, based on a database in Schöier et al. (2005). It is actually 2 orders of magnitude smaller than that of a H_2O maser, and comparable with the pre-shock density of the maser (Elitzur 1992). The H_2O maser is, hence, probably excited in the most strongly compressed part, such as a head part of a bow shock. Emission from that region cannot dominate the integrated SiO emission, since such a region should have a quite limited volume compared to the total post-shock gas.

Site C, by contrast to another site, is not associated with SiO emission. There are 9 maser features, and almost all of them (7 of 9) are highly variable, and only detected in a single epoch. This maser site had been reported in the past VLA observation (Hofner & Churchwell 1996), but the observed position and line-of-sight velocity were slightly different from our detection. All maser features, including that detected by VLA, were closely located at the position of Feldt's star (< 200 mas). Their line-of-sight velocities were little red-shifted from a systemic

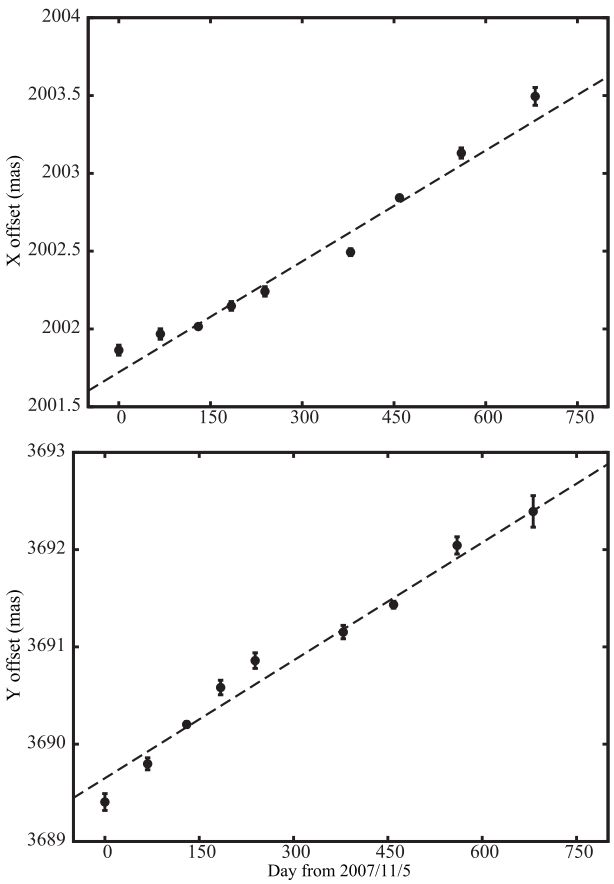

Fig. 2. The internal proper motion of feature C6. Y axes in each panel show the positional offset relative to the phase-referenced feature O1. Both of dashed lines indicate the best-fit linear proper motions.

Table 5. Detected maser features.

Feature	Epoch	$V_{\rm LSR}$ (km s^{-1})	ΔV^* (km s^{-1})	Offset† (mas) X (error)	Y (error)	Peak intensity (Jy beam^{-1})
O1	1	9.36	1.26	0.00 (0.03)	0.00 (0.08)	74.0
	2	9.34	1.69	−0.20 (0.01)	−0.03 (0.02)	75.6
	3	9.26	1.90	−0.38 (0.01)	−0.06 (0.01)	80.3
	4	9.50	2.11	−0.54 (0.01)	−0.08 (0.02)	72.1
	5	9.37	1.47	−0.71 (0.02)	−0.11 (0.04)	63.6
	6	9.33	1.26	−1.12 (0.02)	−0.17 (0.05)	32.0
	7	9.30	1.26	−1.36 (0.01)	−0.21 (0.02)	19.6
	8	9.39	1.05	−1.65 (0.04)	−0.25 (0.11)	21.7
	9	9.26	1.26	−2.01 (0.04)	−0.31 (0.11)	14.2
O2	1	8.72	0.63	−15.90 (0.06)	2.33 (0.17)	10.1
	2	8.70	0.84	−16.24 (0.06)	2.30 (0.10)	5.5
	3	8.63	1.05	−16.51 (0.04)	2.25 (0.10)	7.0
	4	8.65	0.84	−16.63 (0.06)	2.12 (0.15)	5.9
	5	8.74	0.63	−16.85 (0.07)	2.08 (0.17)	5.1
	6	8.48	0.63	−17.16 (0.08)	1.87 (0.25)	3.4
	7	8.46	0.84	−17.20 (0.06)	1.76 (0.14)	3.2
	8	8.76	0.63	−17.69 (0.09)	1.78 (0.23)	2.7
C1	8	17.19	0.63	1954.03 (0.05)	3852.79 (0.14)	5.1
C2	2	15.45	0.63	1984.14 (0.07)	3745.18 (0.12)	4.2
C3	7	12.67	1.69	1944.75 (0.04)	3732.56 (0.08)	3.3
C4	7	12.67	0.84	1946.13 (0.09)	3736.36 (0.21)	1.3
C5	3	11.58	0.63	1998.60 (0.07)	3665.11 (0.17)	2.8
C6	1	11.04	1.05	2001.86 (0.03)	3689.41 (0.09)	27.9
	2	11.02	1.26	2001.77 (0.03)	3689.77 (0.06)	19.8
	3	11.16	1.47	2001.63 (0.01)	3690.14 (0.03)	43.0
	4	11.18	1.68	2001.60 (0.03)	3690.50 (0.07)	56.0
	5	11.27	1.26	2001.54 (0.03)	3690.75 (0.08)	46.9
	6	11.22	1.26	2001.37 (0.02)	3690.98 (0.07)	39.8
	7	11.19	1.47	2001.49 (0.02)	3691.23 (0.04)	28.3
	8	11.08	1.47	2001.48 (0.03)	3691.79 (0.09)	13.7
	9	10.94	1.05	2001.48 (0.06)	3692.09 (0.16)	4.7
C7	7	10.56	0.63	1944.66 (0.09)	3732.89 (0.21)	1.9
C8	3	10.74	0.63	1990.50 (0.05)	3662.93 (0.11)	5.1
	1	9.78	0.63	1978.74 (0.03)	3668.10 (0.08)	22.1
	2	9.76	0.84	1978.48 (0.06)	3668.15 (0.10)	9.9
	3	9.90	0.84	1978.20 (0.03)	3668.34 (0.08)	8.2
	5	10.00	0.63	1977.75 (0.08)	3668.60 (0.20)	3.9
N	2	3.65	1.05	3932.54 (0.05)	4185.95 (0.09)	6.7
	3	2.95	2.95	3932.14 (0.02)	4186.54 (0.04)	18.0
	7	3.82	1.26	3929.04 (0.05)	4184.55 (0.11)	2.9
S1	4	8.23	1.26	4898.62 (0.07)	−1070.77 (0.19)	8.0
	5	8.11	1.05	4898.48 (0.04)	−1070.66 (0.10)	13.7
	6	8.06	1.47	4898.27 (0.05)	−1071.59 (0.15)	12.6
	7	8.03	1.47	4898.35 (0.03)	−1071.68 (0.07)	11.3
	8	8.13	1.05	4898.50 (0.05)	−1071.14 (0.14)	4.7
S2	8	8.13	0.63	4897.28 (0.09)	−1075.02 (0.24)	2.4

* Full width at zero intensity (FWZI) for each maser feature.

† The positions relative to ($18^{\rm h}00^{\rm m}30.^{\rm s}3066$, $-24^\circ04'4.''48649$) (J2000.0).

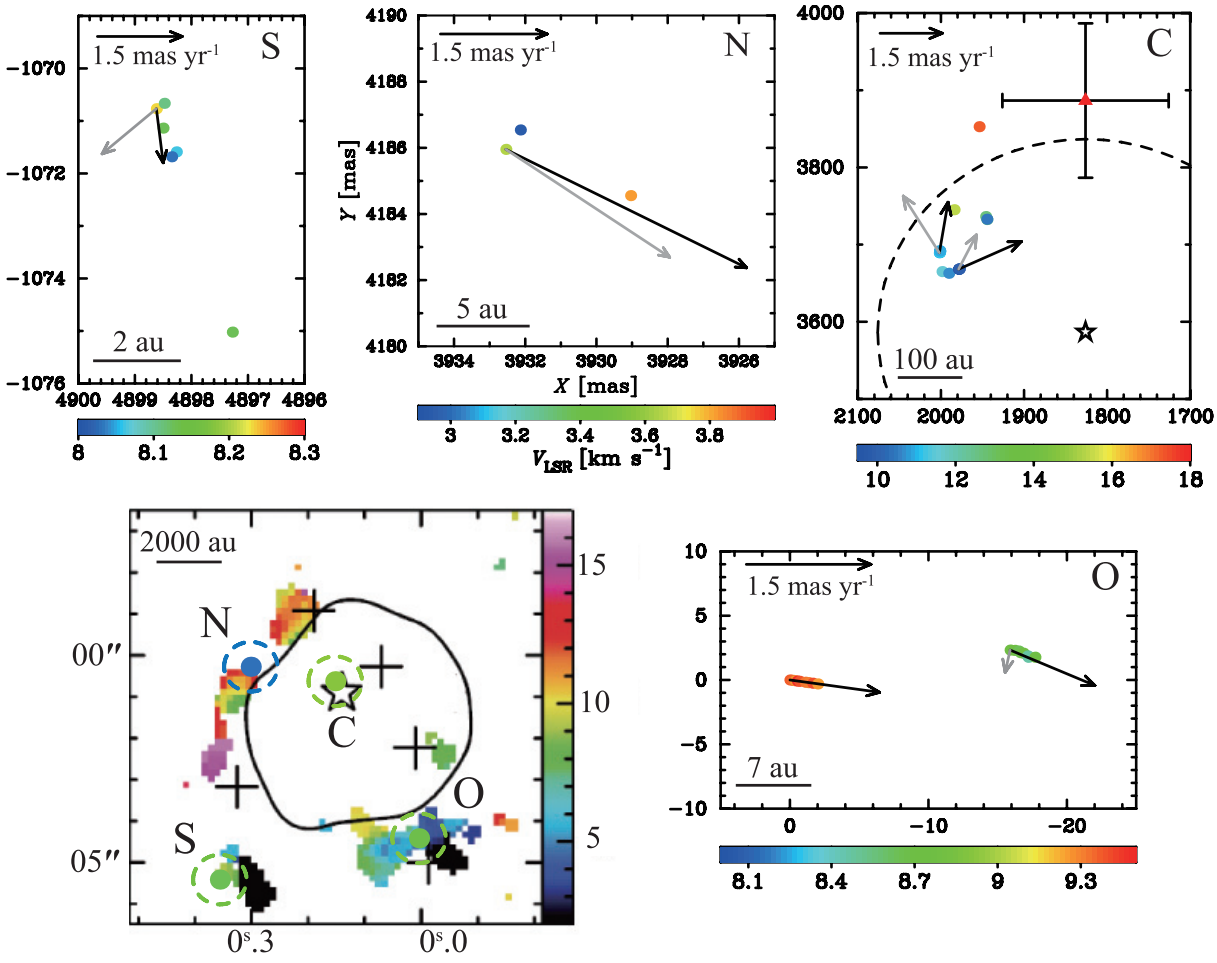

Fig. 3. Overall distribution of maser features. Lower left panel: The locations of 4 maser sites (O, C, N, S) are presented by color points with dashed circles. The coordinate origin is $\alpha_{2000} = 18^{\rm h}00^{\rm m}30\overset{\rm s}{.}3$, $\delta_{2000} = -24°04'0\overset{''}{.}0$. Here, the background color scale, black crosses and contour show the first-moment map of SiO $J = 8$–7 emission, 875 μm dust cores and 3 mm continuum image (0.1 Jy beam^{-1}) from Hunter et al. (2008), respectively. The star marks the positions of Feldt's star, $\alpha_{2000} = 18^{\rm h}00^{\rm m}30\overset{\rm s}{.}44$, $\delta_{2000} = -24°04'0\overset{''}{.}9$. Other 4 panels: Detailed distributions of maser features are shown. Here, each point indicates the detected maser feature. Each axis shows the relative coordinate from the phase-referenced maser feature, O1, in units of mas. Absolute and internal proper motions are written in black and grey arrows, respectively. Red triangle with error bar in site C (upper right panel) is the maser detected by Hofner and Churchwell (1996). Here, the star marks the position of Feldt's star again and its error is presented by a dashed circle of 250 mas diameter (200 from positional error and 50 from PSF, see Feldt et al. 2003). The color represents $V_{\rm LSR}$ (km s^{-1}) for all 5 panels in the scale of the associated color bars.

velocity of 9 km s^{-1} (e.g., Hunter et al. 2008), and clearly different from that of OH masers seen at the same position (Stark et al. 2007).

Highly blue-shifted (~ -35 km s^{-1}) OH masers are thought to be excited in an expanding neutral shell or strong outflow (the former in Stark et al. 2007, the latter in Zijlstra et al. 1990). They seem to be located on the foreground of the ionized shell in either case. The kinematic difference strongly invokes the distinct origins of OH and H_2O masers. Such a nearly located, but strictly distinct displacement of these two maser, is quite natural if we consider different excitation conditions again, and it had been actually observed for several regions (Forster & Caswell 1989). Taking into account this situation, we propose that this H_2O maser site is just located inside an ionized shell, and excited in a remnant of dense circumstellar structure, such as an accretion disk. The extremely young dynamical age of the UCH II region ($\sim$600 yr) well supports the presence of such a remnant; the crescent-like distribution and velocity field can actually be explained by a simple ring model (see sub-subsection 5.2.2).

5. Discussion

5.1. *Validity of New Distance*

The newly estimated distance of 1.28 kpc is much smaller than the previously reported distances ($>$ 1.9 kpc). This is mainly because almost all of the past measurements were made kinematically. The kinematic distance essentially depends on the galactic rotation model and the accuracy of determining the rotation velocity of the source. If it is the case that the target source has an unknown, non-negligible velocity component aside from the galactic rotation, the kinematic distance is no longer reliable, in principle. This type of systematic error is more and more significant, especially for a source near

Table 6. Recalculated stellar parameters.

Parameter	Original value	Modified value	References*
$N_{\rm L}$ (s^{-1})	4.5×10^{48}	1.6×10^{48}	(1)
$L_{\rm FIR}$ ($L_\odot$)	3.0×10^5	7.3×10^4	(1)
Sp Type (radio)	O7	O8.5	(1), (2)
Sp Type (FIR)	O6	O8	(1), (2)
M_* ($M_\odot$)	~ 40	~ 25	(3)
$\dot{P}_{\rm wind}$ ($M_\odot$ km s^{-1} yr^{-1})	—	2.5×10^{-3}	(4)

* (1): Wood and Churchwell 1989, (2): Panagia 1973, (3): Vacca et al. 1996, (4):this work.

the galactic center direction. In the case of our source ($l = 5.^\circ89$), only a few km s^{-1} offset along the line of sight can cause an error of ~ 1 kpc.

Reid et al. (2009) has first analyzed the galactic rotation based on the distances of 18 star-forming regions, which are estimated only from trigonometric parallaxes of masers derived from VLBA and VERA observations. Their new analysis indicates that commonly used kinematic distances are generally overestimated, sometimes by factors greater than 2, which is just our case. A similar result has already been reported in other VERA observation [G14.33−0.64, the measured distance ~ 1.1 kpc, $l = 14.^\circ33$ (Sato et al. 2010b)]. Our result seems to be very consistent with the hypothesis in Sato et al. (2010b) that the Sagittarius spiral arm, in which G5.89−0.39 and G14.33−0.64 are thought to be located, lies at a closer distance (~ 1 kpc) from the Sun compared to the previous value (2–3 kpc). Of course, more large samples must be required to confirm it.

A progressive galactic simulation in Baba et al. (2009) also suggests that star-forming regions and young stars in a spiral arm have significant non-circular motions of up to 30 km s^{-1}. If their calculation is correct, a kinematic distance intrinsically has a large systematic error of ~ 2–3 kpc. With these contexts, the significant difference between the kinematic distance and our new distance can be attributed to the systematic error in the kinematic distance.

ACW98 derived a source distance of 2.0 kpc from the expansion of the ionized shell, but it is still highly model-dependent (see sub-subsection 5.2.3). Consequently, our new distance, which has no model dependency, is thought to be the most reliable distance of G5.89−0.39.

5.2. *Physical Parameters and High-Mass Star Formation in G5.89−0.39*

Because of a significant modification of the distance to G5.89−0.39, we first recalculated the physical parameters that had been previously reported based on the new distance. Tables 6 to 9 summarize the recalculated parameters. Each table contains both the original and modified values with reference papers. Detailed explanations for the listed parameters are given in related subsections and captions.

5.2.1. *Evolution of the O-type protostar*

Table 6 lists the properties of Feldt's star. We derived the stellar spectral type in the same manner as in Wood and Churchwell (1989). We first estimated the excitation parameter of the source from the radio continuum emission (see also Krutz et al. 1994). This was simply converted to the flux of Lyman continuum photons ($N_{\rm L}$) and spectral type (Sp type), comparing the stellar models in Panagia (1973). In the second, we used the total far-infrared luminosity ($L_{\rm FIR}$). $L_{\rm FIR}$ can be a good measure of the bolometric luminosity for deeply embedded sources. Because of the low spatial resolution, $L_{\rm FIR}$ may include several contributions from other objects around the UCH II region, and hence this gives the upper limit of the source luminosity.

The derived spectral types are almost consistent, and indicate late O-type stars (O8−O8.5 ZAMS). The expected stellar mass, M_*, is about $\sim 25\,M_\odot$ (e.g., Vacca et al. 1996). This is a roughly half the value of the previously reported O5 ZAMS (or O5V) star. Feldt et al. (2003) tested such an early spectral type by the model fitting of the mid-infrared color ($K_{\rm s}$ and L' bands). However, their fitting is based on a distance of 1.9 kpc, and if we adopt the new distance and appropriate extinction value, all of O type stellar models that are later than O5 can move into the range of the L' band excess reported in Feldt et al. (2003).

The line ratio of the He I triplet at 2.11 μm to Brγ also supports the existence of a late O-type star. Hanson, Luhman, and Rieke (2002) have observationally determined the upper limit of this ratio as being 0.02 for G5.89−0.39, and indicated that this value is clearly smaller than the value expected for a star earlier than the O7 type. Puga et al. (2006) actually detected 2.11 μm He I emission with VLT. Although they suggested a rather early O star (< O7), detection only at the location of Feldt's star also ruled out a star earlier than O7, because such an early type star could fully ionize all He atoms, and provide a constant line ratio throughout a UCH II region (e.g., Osterbrock 1989). This seems to be a reliable constraint, since the line ratio is fully independent of the source distance. Consequently, the new spectral type of O8−O8.5 seems to be reasonable.

As can be seen in table 6, we also estimated the momentum rate of the stellar wind ($\dot{P}_{\rm wind}$). It was calculated from the pressure balance at the inner surface of the ionized shell. We simply assumed that a spherically-symmetric wind, and that the thermal pressure of ionized gas was balanced with $\dot{P}_{\rm wind}$ per unit area. Although the detailed properties of the mass-loss activity at the ZAMS stage are still unknown, the estimated $\dot{P}_{\rm wind}$ is ten-times larger than that of a dwarf star of $\sim 25\,M_\odot$ (Sternberg et al. 2003 and reference therein). The wind velocity is generally determined by gravitational force at the launching point of the wind, and it is thought to be of

Table 7. Recalculated parameters of the UCH II region.

Parameter	Original value	Modified value	Reference*
$n_{\rm e}$ (cm^{-3})	2.4×10^5	3.2×10^5	(1)
$R_{\rm i}/R_{\rm e}$ (AU)	1900 / 5200	1200 / 3300	(2)
$\upsilon_{\rm shell}^{\dagger}$ (km s^{-1})	39	25	(2)
$t_{\rm dyn}$ (yr)	600	600	(2)
$E_{\rm Therm}$ (10^{45} erg)	—	0.7	(3)
$E_{\rm Kin}$ (10^{45} erg)	—	1.2	(3)
$P_{\rm shell}$ ($M_\odot$ km s^{-1})	—	5.6	(3)
$M_{\rm env}$ ($M_\odot$)	300	123	(4)
$n_{\rm env}$ (cm^{-3})	5.3×10^6	8.0×10^6	(4)
$T_{\rm env}$ (K)	40–140	40–140	(5)

* (1): Wood and Churchwell 1989, (2):ACW98, (3):this work, (4): Tang et al. 2009, (5): Su et al. 2009.
† Tangential expansion derived from the angular expansion rate.

Table 8. Parameters of the E–W outflow (CO $J = 1$–0) from Watson et al. (2007).

Parameter	Original value		Modified value	
$t_{\rm dyn}$ (yr)	7700		5000	
	Blue lobe	Red lobe	Blue lobe	Red lobe
$\upsilon_{\rm flow}$* (km s^{-1})	–15.0–3.2	13.2–25.0	–15.0–3.2	13.2–25.0
M ($M_\odot$)	123	116	50	48
$E_{\rm kin}$ (10^{46} erg)	6.4	5.3	2.6	2.2
P (10^2 $M_\odot$ km s^{-1})	9.0	8.0	3.7	3.3
$\dot{M}$ ($10^{-3} M_\odot$ yr^{-1})	16.0	15.0	10.0	9.6
$\dot{P}$ ($10^{-2} M_\odot$ km s^{-1} yr^{-1})	12.0	10.0	7.7	6.4
$L_{\rm mech}$ ($L_\odot$)	68.0	56.0	44.0	36.0

* Integrated velocity range.

Table 9. Parameters of the inner high velocity outflow (CO $J = 3$–2) from Klaassen et al. (2006).

Parameter	Original value*		Modified value	
$t_{\rm dyn}$ (yr)	2000		1300	
	Blue lobe	Red lobe†	Blue lobe	Red lobe†
$\upsilon_{\rm flow}$‡ (km s^{-1})	−66.0	78.0	−66.0	78.0
M ($M_\odot$)	2.7	0.6	1.1	0.3
$E_{\rm kin}$ (10^{46} erg)	1.5	0.3	0.6	0.1
P ($M_\odot$ km s^{-1})	55.9	12.0	22.0	4.9
$\dot{M}$ ($10^{-4} M_\odot$ yr^{-1})	13.5	3.0	8.5	1.9
$\dot{P}$ ($10^{-2} M_\odot$ km s^{-1} yr^{-1})	2.8	0.6	2.7	0.4
$L_{\rm mech}$ ($L_\odot$)	59.0	11.5	38.0	7.4

* Inclination of outflow axis which has been originally assumed as 45° is ignored.
† Absorption features seen in the red lobe have not been corrected in Klaassen et al. (2006).
‡ The maximum velocities.

the same order between ZAMS and the dwarf stage. This is about 2.0×10^3 km s^{-1} for a 25 $M_\odot$ dwarf (e.g., Smith et al. 2002). In this case, the mass-loss rate is on the order of $10^{-6} M_\odot$ yr^{-1}, and of cource, ten-times larger than the value of dwarfs. One possible explanation for this excess may be a larger stellar radius of a very young ZAMS star that is still under contraction. This could cause relatively weak surface gravity, and might aid the mass-loss activity.

Recent theoretical work in Hosokawa and Omukai (2009) calculated the detailed stellar evolution via spherically-symmetric mass accretion. They have shown that a large entropy supply under high accretion rates ($> 10^{-4}$ $M_\odot$ yr^{-1}) onto a proto-stellar surface prevents the contraction of a protostar, and causes a large stellar radius ($\sim 100\, R_\odot$).

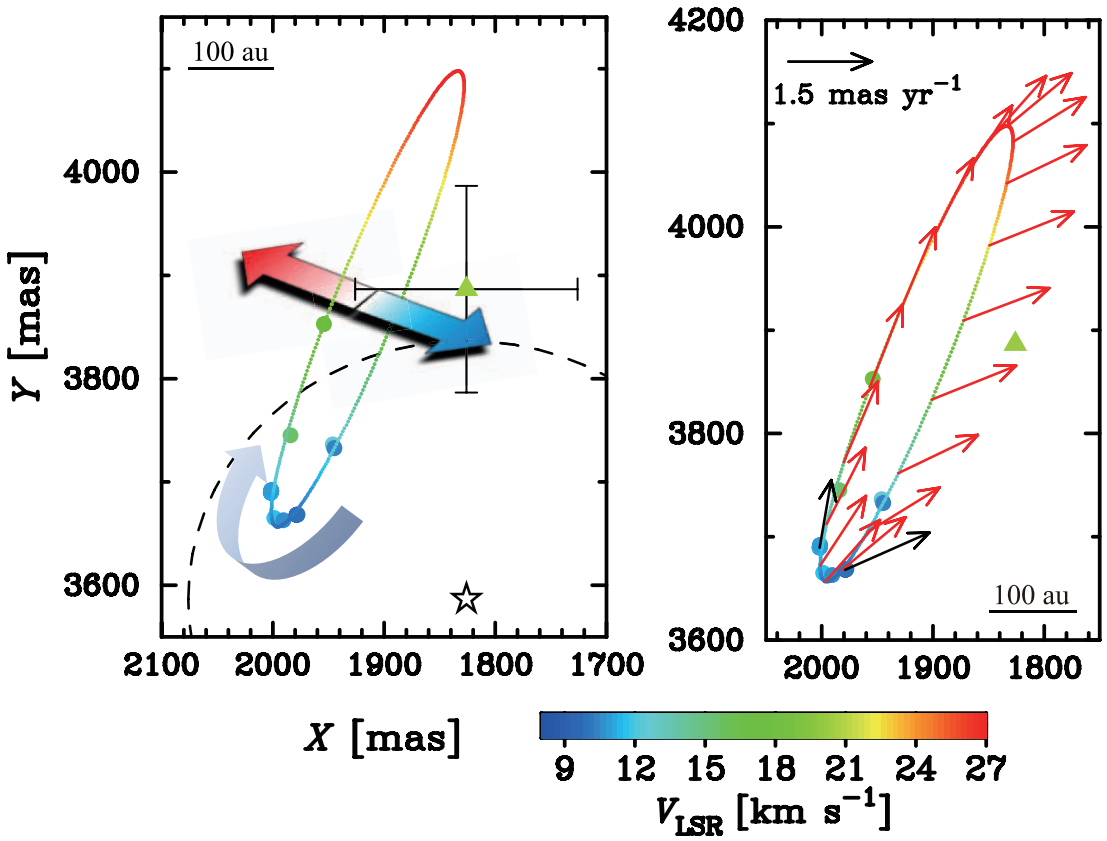

Fig. 4. Left panel shows the best-fit ring model superposed on the maser distribution in figure 3. Curved arrow represents rotational direction. The red and blue arrows show a same geometry as red and blue lobe of E–W outflow. The inclination of the ring is consistent with this outflow geometry. Right panel shows velocity field of the ring. Red and black arrows show expected proper motion vectors of the ring and observed vectors, respectively. These motions contain both of the systemic velocity of G5.89−0.39 offset from the galactic rotation and migration velocity of the ring.

Hosokawa, Yorke, and Omukai (2010) treated the case of cold-disk accretion, and have suggested that the expected evolution is qualitatively the same as the spherically-symmetric case after $10\,M_\odot$. Realistic mass accretion should correspond to some intermediate state between these two extreme cases, as they pointed out.

The most important product of their evolutional track is delayed hydrogen burning. The resultant young high mass (proto-)star with a large radius and limited UV photons can explain the highly luminous, but low-effective temperature source, which has no detectable H II region (e.g., Beuther et al. 2007, Furuya & Shinnaga 2009). If Feldt's star is just after hydrogen ignition, the maximum accretion rate in the main accretion phase is estimated to be $\sim 10^{-3}\,M_\odot\,\mathrm{yr}^{-1}$ from $\sim 25\,M_\odot$ based on their calculations. This assumption may mean that Feldt's star is a quite rare sample, but it seems to be very consistent with the extraordinarily young dynamical age of the UCH II region. If this is the case, and we assume steady mass accretion, the time required to form Feldt's star is simply $\sim 2.5 \times 10^4$ yr.

5.2.2. Maser morphology near the feldt's star: a possible partial ring

The newly detected crescent-like structure of water masers may also suggest the youth of the source. As we mention above, the maser clumps at site C can be associated with circumstellar remnant gas. Their alignment and velocity field are actually fitted by the Keplerian rotating and expanding ring model in Uscanga et al. (2008). The fitting parameters are the central position of a ring (x_0, y_0), radius R, the inclination from the celestial plane, i, the position angle of the apparent major axis measured from east toward north, θ, the expansion (or infalling) velocity, $\upsilon_{\rm exp}$, and the velocity of the source (υ_x, υ_y, υ_z). Here, z means a line-of-sight direction. We regarded Feldt's star as a central source of the ring; in turn, its mass was fixed to be $25 M_\odot$. Thus, the Keplerian rotation velocity depended on only R.

We performed a model fit with a standard χ^2 fitting. First, the spatial distribution of 9 (our detection) + 1 (VLA detection) maser features was fitted by x_0, y_0, R, i, θ, and then υ_x, υ_y, υ_z were determined from the velocity field of the masers. It should be noted that υ_x and υ_y are more uncertain than υ_z, because there are only 2 available proper-motion vectors. Table 10 and figure 4 show the best-fitted parameters and estimated ring superposed on the maser alignment, respectively.

The best-fitted ring is almost edge-on, and its position angle is roughly in the north–sorth direction. It is noteworthy that this geometry matches well the largest outflow, which has a position angle of nearly linear alignment from east (red lobe) to

Table 10. The best fit parameters of the ring model.

Parameter	Best fit (error)*
x_0 (mas)	1914.6 (0.5)
y_0 (mas)	3877.2 (0.8)
R (mas)	235.2 (1.2)
θ (°)	110.5 (0.2)
$i^{\dagger}$ (°)	+83.0 (0.2)
$\upsilon_{\rm exp}$ (km s^{-1})	−1.2 (0.8)
υ_x (km s^{-1})	−6.5 (1.5)
υ_y (km s^{-1})	6.4 (1.1)
υ_z (km s^{-1})	18.6 (0.4)

* Formal 4 σ error of χ^2 fittings.
† Western edge is on the far side.

Table 11. Divided velocity components.

Migration velocities of Feldt's star			
(υ_x, υ_y, υ_z)	6.3* (0.3)	6.0 (0.3)	9.6 (0.0)
Non-circular motion of G5.89−0.39			
(υ'_x, υ'_y, υ'_z)	−12.8 (1.8)	0.4 (1.4)	4.7 (0.4)
(U, V, W)	5.4 (1.6)	−5.5 (2.4)	11.3 (2.4)

* Velocities are in the units of km s^{-1}.

west (blue lobe) (see below). The center of the ring is slightly offset from Feldt's star (1826 mas, 3587 mas), but it can be within the ring if we take into account an $\sim$200 mas error. The small and negative expansion velocity means that the ring is slowly infalling.

Class II CH_3OH masers, which are believed to trace an accretion disk around HMPOs (e.g., Bartkiewicz et al. 2009 and reference therein), are not seen in the G5.89−0.39 region. This may be consistent with the fact that Class II CH_3OH maser emission trace the pre-UCH II stage (e.g., Walsh et al. 1998; Codella & Moscadelli 2000). On the other hand, a disk-like structure traced by 22 GHz H_2O masers has actually been reported in some sources. Imai et al. (2006) have especially found an infalling-rotating maser disk, which is a similar case to ours, for early B-type HMPO. Torrelles et al. (1996) reported a H_2O maser disk candidate in Cepheus A HW2, which had almost the same radius ($\sim$300 AU) as in our case. If crescent-like masers actually trace an accretion disk (or its remnant), it is a clear indicative of a quite youthful O-type object that is at least before complete disk evaporation.

We finally discuss the velocity field. The 3D motion of the ring (υ_x, υ_y, υ_z) still includes the non-circular (peculiar) motion of the G5.89−0.39 system (recall subsections 4.3 and 5.1). To divide these contributions, we now assume 2 conditions, as follows: (1) Feldt's star was initially located at the center of the radio shell, but migrated to the current position in the dynamical time of the shell, (2) the ring moved together with the star. The possibility of stellar migration was already discussed in Feldt et al. (2003). This motion corresponds to be a proper motion of about 1.04 ± 0.30 mas yr^{-1} and 0.98 ± 0.28 mas yr^{-1} in the X and Y directions, respectively. In contrast, the migration velocity along a line of sight ($\sim$9.6 km s^{-1}) can be obtained from $\upsilon_z - V_{\rm LSR}$. The 3D motion of the partial ring can be eventually divided into the migration motion of Feldt's star and the systemic peculiar motion of G5.89−0.39. These divided values are presented in table 11, where the line-of-sight component of the peculiar motion ($\sim$4.7 km s^{-1}) was also extracted from $V_{\rm LSR}$ using the galactic rotation model in Hou et al. (2009).

The peculiar motion of the system has also been shown in the (U, V, W) frame at the same time. Here, U is toward the galactic center from the source position, V is along the galactic rotation at the local place, W is perpendicular to the galactic plane and toward the north galactic pole. The magnitude of the non-circular component, $\sim$14 km s^{-1}, is sufficient within the theoretically predicted range (see subsection 5.1 again).

5.2.3. Anisotropic expansion of UCH II region

Table 7 summarizes the parameters of the UCH II region. The upper seven rows present the electron density, $n_{\rm e}$, the inner / outer radius of the radio shell, $R_{\rm i}$ / $R_{\rm o}$, the expansion velocity, $\upsilon_{\rm shell}$, the dynamical age, $t_{\rm dyn}$, the thermal energy of ionized gas, $E_{\rm therm}$, the kinetic energy, $E_{\rm kin}$, and the total momentum of shell expansion, $P_{\rm shell}$. The lower three rows contain the parameters of the surrounding dense envelope. The envelope mass, $M_{\rm env}$, and the density, $n_{\rm env}$, were obtained from SMA observations of the submillimeter dust continuum (Tang et al. 2009), and its size scale is roughly 2×10^4 AU. Especially, the envelope temperature, $T_{\rm env}$, was derived from an excitation analysis of the CH_3CN (J = 12–11) line by Su et al. (2009), and hence does not depend on the distance. They found a temperature gradient in the range given in the table.

The overall properties of the ionized region have not changed drastically, except for the expansion velocity, which was calculated from an angular expansion rate of 4 ± 1 mas yr^{-1} in ACW98. Even if ionized gas is in a free expansion state, its expansion velocity should be almost equal to the sound speed of ionized gas ($\sim$13 km s^{-1} at 10^4 K). This suggests that only half of the total momentum can be thermally provided, and the shell must require another source of momentum input. If we attribute it to a spherically symmetric stellar wind, discussed in sub-subsection 5.2.1, the required time is about 1000 yr. Moreover, if the momentum of photons from Feldt's star is added, the total momentum of the shell could be provided during $t_{\rm dyn}$.

ACW98 have determined the source distance in comparison between the angular expansion rate and the line width of the radio recombination lines under several assumptions about how the shell expansion contributes to the line width. We now have a more accurate distance and, in turn, we can estimate a residual contribution to the line width, which offsets from spherical expansion. This value is $\sim$50 km s^{-1}, based on their analysis. This is twice as large as the tangential expansion, and nearly consistent with highly blue-shifted OH masers in front of the shell.

This highly anisotropic expansion could be explained by the idea proposed by Hunter et al. (2008), where an outflow from SMA1, which is a luminous dust core near Feldt's star, had been going across north to south, and it was disrupted after formation of the UCH II region. If this is the case, the ionization of intrinsically expanding gas within the outflow can

give a plausible explanation for high-velocity ionized gas, and hence the observed anisotropy.

5.2.4. Outflow nature

The revised properties of the outflowing gas in G5.89−0.39 are listed in tables 8 and 9. Table 8 lists the parameters of CO ($J = 1$–0) emission, which trace the outer extended flow (Watson et al. 2007), and table 9 presents that of the inner high-velocity flow that has been detected in CO ($J = 3$–2) emission (Klaassen et al. 2006). Each table contains the dynamical age, $t_{\rm dyn}$, outflow velocity (or velocity ranges), $\upsilon_{\rm flow}$, outflow mass, M, kinetic energy, $E_{\rm kin}$, momentum, P, outflow rate, $\dot{M}$, momentum rate, $\dot{P}$, and mechanical luminosity, $L_{\rm mech}$. We note that the effect of inclination is not corrected in these tables, although Klaassen et al. (2006) originally assumed an inclination of 45°.

The largest outflow given in table 8 is thought to be driven by Feldt's star, and extends just in the east–west direction (see figure 2 in Watson et al. 2007). The total mass, measured from CO ($J = 1$–0), is $\sim 100\,M_\odot$, and greatly exceeds the source mass. Such an extremely massive outflow is often observed toward a high-mass star-forming region (e.g., López-Sepulcre et al. 2009). The origin of large mass is an unsolved problem (e.g., Churchwell 1997).

A detailed driving mechanism of a protostellar outflow is still under discussion; however Machida, Inutsuka, and Matsumoto (2008) have shown that a high-velocity jet and molecular outflow (hereafter called intrinsic outflows) are distinctly driven in their MHD simulation as natural products of magnetized core collapse and mass accretion via a rotating disk. This is very consistent with a case of nearby low-mass star formation, and seems to be applicable for the high-mass case, as long as objects are formed by gravitational collapse and mass accretion. The energy source of intrinsic outflows is gravitational energy, which is transformed into outflow energy mediated by magnetic fields. In this point of view, the total outflow mass of intrinsic outflows cannot exceed that of the central object at a driving point. Clearly, much of the outflow mass arises from material entrained far from the driving source. Quantitatively, observations of outflows from massive young protostellar objects show that the entrained mass is on the order of 4% of the core mass surrounding the central protostar (e.g., Beuther et al. 2002b). This relation suggests that the parent core for the forming cluster containing Feldt's star contained about $\sim 2500\,M_\odot$.

On the other hand, if we assume the ratio of the outflow to the accretion rate to be $\sim 10\%$ from theoretical work (e.g, Pelletier & Pudritz 1992), the total mass of intrinsic outflows for Feldt's star is $\sim 2.5\,M_\odot$, following the discussion in subsubsection 5.2.1. This is comparable to the mass of the CO ($J = 3$–2) outflow, which traces the inner hot and high-velocity outflow (see table 9). If we consider the momentum transport from the CO ($J = 3$–2) outflow to the CO ($J = 1$–0) outflow, the required time is 2.3×10^4 yr. This is consistent with the formation time of Feldt's star, estimated above, and is clearly larger than the dynamical age of outflow, which was obtained from an extent divided by a current velocity. We note that this time scale should be a lower limit, since the mass and momentum of the CO ($J = 3$–2) outflow is the sum of the east–west flow from Feldt's star and north–south flow from SMA1. They have been unresloved in the single-dish data in Klaassen et al. (2006), and actually a significant fraction of high-velocity emission arises from the latter (see high resolution images in Hunter et al. 2008).

The fact that a commonly used dynamical time underestimates the actual outflow age has already been pointed out in the case of low-mass objects (Parker et al. 1991), and we suggest that it can occur in the case of too-massive outflow in high-mass star formation, which includes a large entrained mass. We should consequently be careful that an observationally estimated outflow rate, which often reaches $10^{-2} M_\odot\,{\rm yr}^{-1}$ for a high-mass star, is also overestimated by an order of magnitude. This appears to be reasonable because Hosokawa and Omukai (2009) have predicted that a large accretion luminosity must prevent steady accretion in the case of such a too-large accretion rate. Detailed information about a termination of high-velocity inner flow is quite useful to confirm these discussions. This would be obtained from direct measurements of the proper motions of outflow lobes with ALMA.

6. Conclusion

The distance of G5.89−0.39 is newly estimated to be $1.28^{+0.09}_{-0.08}$ kpc from the annual parallax measurement with VERA. This is 2/3 of the previously known value, but it is very reasonable if we take into account the small galactic longitude of $\sim 5.^\circ89$, and a recent theoretical prediction about non-circular motions of star-forming regions.

Rescaled physical parameters based on the new distance give us several in-depth natures of high-mass star formation in G5.89−0.39, as follows:

(1) The ionizing star is a rather later-type ZAMS than the previously believed type of O5. Spectral types of O8–O8.5 means that the UCH II region is excited by a not-so-massive and standard O-type object. The expected accretion rate is $\sim 10^{-3} M_\odot\,{\rm yr}^{-1}$, based on the extremely young age of the ionized shell and a detailed evolutional track of a massive protostar under a high accretion rate. The resultant formation time is about $\sim 2.5 \times 10^4$ yr in this case.

(2) The detected maser alignment at the O-star can be fitted by an infalling Keplarian ring; its inclination and position angle are also consistent with the east–west orientation of the strong outflow. It seems to trace accretion disk (or its remnant), and suggests remarkable youth of the O-star, which is before complete evaporation of the circumstellar structure.

(3) Reconsideration of the outflow nature suggests that a large portion of the outflow mass should be entrained from a massive envelope. A commonly used dynamical time should significantly underestimate the actual outflow age, just the same as in the low-mass cases. This also causes an overestimate of the outflow rate by an order of magnitude. Direct observations of momentum transportation from intrinsic outflow to outer entrained flow are required to confirm this. This might be achieved by proper-motion measurements of the outflow lobe with ALMA.

We finally emphasize that G5.89−0.39 is one of the nearest targets suitable for investigating individual high-mass star formation, and the evolution of core-scale clusters, including an O-type object.

We would like to thank all members of the VERA project for their assistance in observations and data analyses. We also thank the refree for helpful comments. This work was financially supported by the Research Fellowships of the Japan Society for the Promotion of Science (JSPS).

References

Acord, J. M., Churchwell, E., & Wood, D. O. S. 1998, ApJ, 495, L107 (ACW98)
Acord, J. M., Walmsley, C. M., & Churchwell, E. 1997, ApJ, 475, 693
Baba, J., Asaki, Y., Makino, J., Miyoshi, M., Saitoh, T. R., & Wada, K. 2009, ApJ, 706, 471
Bartkiewicz, A., Szymczak, M., van Langevelde, H. J., Richards, A. M. S., & Pihlström, Y. M. 2009, A&A, 502, 155
Beuther, H., Schilke, P., Sridharan, T. K., Menten, K. M., Walmsley, C. M., & Wyrowski, F. 2002b, A&A, 383, 892
Beuther, H., Walsh, A. J., & Longmore, S. N. 2009, ApJS, 184, 366
Beuther, H., Walsh, A., Schillke, P., Sridharan, T. K., Menten, K. M., & Wyrowski, F. 2002a, A&A, 390, 289
Beuther, H., Zhang, Q., Hunter, T. R., Sridharan, T. K., & Bergin, E. A. 2007, A&A, 473, 493
Breen, S. L., Caswell, J. L., Ellingsen, S. P., & Phillips, C. J. 2010, MNRAS, 406, 1487
Chikada, Y., Kawagudhi, N., Inoue, M., Morimoto, M., Kobayashi, H., & Mattori, S. 1991, in Frontiers of VLBI, ed. H. Hirabayashi et al. (Tokyo: Universal Academy Press), 79
Choi, Y. K., et al. 2008, PASJ, 60, 1007
Churchwell, E. 1997, ApJ, 479, L59
Codella, C., & Moscadelli, L. 2000, A&A, 362, 723
Dehnen, W., & Binney, J. J. 1998, MNRAS, 298, 387
Elitzur, M. 1992, ARA&A, 30, 75
Feldt, M., et al. 2003, ApJ, 599, L91
Forster, J. R., & Caswell, J. L. 1989, A&A, 213, 339
Furuya, R. S., & Shinnaga, H. 2009, ApJ, 703, 1198
Hachisuka, K., et al. 2006, ApJ, 645, 337
Hanson, M. M., Luhman, K. L., & Rieke, G. H. 2002, ApJS, 138, 35
Hirota, T., et al. 2007, PASJ, 59, 897
Hirota, T., et al. 2008, PASJ, 60, 961
Hofner, P., & Churchwell, E. 1996, A&AS, 120, 283
Honma, M., et al. 2003, PASJ, 55, L57
Honma, M., et al. 2007, PASJ, 59, 889
Honma, M., et al. 2008a, PASJ, 60, 935
Honma, M., Tamura, Y., & Reid, M. J. 2008b, PASJ, 60, 951
Hosokawa, T., & Omukai, K. 2009, ApJ, 691, 823
Hosokawa, T., Yorke, H. W., & Omukai, K., 2010, ApJ, 721, 478
Hou, L. G., Han, J. L., & Shi, W. B. 2009, A&A, 499, 473
Hunter, T. R., Brogan, C. L., Indebetouw, R., & Cyganowski, C. J. 2008, ApJ, 680, 1271
Iguchi, S., Kurayama, T., Kawaguchi, N., & Kawakami, K. 2005, PASJ, 57, 259
Imai, H., Omodaka, T., Hirota, T., Umemoto, T., Sorai, K., & Kondo, T. 2006, PASJ, 58, 883
Kawaguchi, N., Sasao, T., & Manabe, S. 2000, in Proc. SPIE, 4015, Radio Telescopes, ed. H. R. Butcher (Washington: SPIE), 544
Klaassen, P. D., Plume, R., Ouyed, R., & von Benda-Beckmann, A. M. 2006, ApJ, 648, 1079
Kobayashi, H., et al. 2008, IAU Symp. 248, 148
Krumholz, M. R., Klein, R. I., McKee, C. F., Offner, S. S. R., & Cunningham, A. J. 2009, Science, 323, 754
Kurtz, S., Churchwell, E., & Wood, D. O. S. 1994, ApJS, 91, 659
López-Sepulcre, A., Codella, C., Cesaroni, R., Marcelio, N., & Walmsley, C. M. 2009, A&A, 499, 811
Ma, C., et al. 1998, AJ, 116, 516
Machida, M. N., Inutsuka, S., & Matsumoto, T. 2008, ApJ, 676, 1088
Moellenbrock, G. A., Claussen, M. J., & Goss, W. M. 2009, ApJ, 694, 192
Motogi, K., et al. 2008, MNRAS, 390, 523
Nakagawa, A., et al. 2008, PASJ, 60, 1013
Osterbrock, D. E. 1989, Astrophysics of Gaseous Nebulae and Active Galactic Nuclei (Mill Valley: University Science Books)
Panagia, N. 1973, AJ, 78, 929
Parker, N. D., Padman, R., & Scott, P. F. 1991, MNRAS, 252. 442
Pelletier, G., & Pudritz, R. E., 1992, ApJ, 394, 117
Petrov, L., Kovalev, Y. Y., Fomalont, E., & Gordon, D. 2005, AJ, 129, 1163
Puga, E., Feldt, M., Alvarez, C., Henning, T., Apai, D., Coarer, E. L., Chalabaev, A., & Stecklum, B. 2006, ApJ, 641, 373
Reid, M. J., et al. 2009, ApJ, 700, 137
Sato, M., et al. 2008, PASJ, 60, 975
Sato, M., Hirota, T., Reid, M. J., Honma, M., Kobayashi, H., Iwadate, K., Miyaji, T., & Shibata, K. M. 2010b, PASJ, 62, 287
Sato, M., Reid, M. J., Brunthaler, A., & Menten, K. M. 2010a, ApJ, 720, 1055
Schöier, F. L., van der Tak, F. F. S., van Dishoeck, E. F., & Black, J. H. 2005, A&A, 432, 369
Smith, L. J., Norris, R. P. F., & Crowther, P. A. 2002, MNRAS, 337, 1309
Stark, D. P., Goss, W. M., Churchwell, E., Fish, V. L., & Hoffman, I. M. 2007, ApJ, 656, 943
Sternberg, A., Hoffmann, T. L., & Pauldrach, W. A. 2003, ApJ, 599, 1333
Su, Y.-N., Liu, S.-Y., Wang, K.-S., Chen, Y.-H., & Chen, H.-R. 2009, ApJ, 704, L5
Takami, M., Takakuwa, S., Momose, M., Hayashi, M., Davis, C. J., Pyo, T.-S., Nishikawa, T., & Kohno, K. 2006, PASJ, 58, 563
Tang, Y.-W., Ho, P. T. P., Girart, J. M., Rao, R., Koch, P., & Lai, S.-P. 2009, ApJ, 695, 1399
Torrelles, J. M., et al. 2010, MNRAS, 410, 627
Torrelles, J. M., Gómez, J. F., Rodríguez, L. F., Curiel, S., Ho, P. T. P., & Garay, G. 1996, ApJ, 457, L107
Uscanga, L., Gómez, Y., Raga, A. C., Cantó, J., Anglada, G., Gómez, J. F., Torrelles, J. M., & Miranda, L. F. 2008, MNRAS, 390, 1127
Vacca, W. D., Garmany, C. D., & Shull, J. M. 1996, ApJ, 460, 914
Walsh, A. J., Burton, M. G., Hyland, A. R., & Robinson, G. 1998, MNRAS, 301, 640
Watson, C., Churchwell, E., Zweibel, E. G., & Crutcher, R. M. 2007, ApJ, 657, 318
Wood, D. O. S., & Churchwell, E. 1989, ApJS, 69, 831
Zijlstra, A. A., Pottasch, S. R., Engels, D., Roelfsema, P. R., te Lintel Hekkert, P., & Umana, G. 1990, MNRAS, 246, 217
Zinnecker, H., & Yorke, H. W. 2007, ARA&A, 45, 481